Chiral magnetohydrodynamic turbulence in core-collapse supernovae

Youhei Masada,[1] Kei Kotake,[2] Tomoya Takiwaki,[3] and Naoki Yamamoto[4]

[1]*Department of Science Education, Aichi University of Education, Kariya 448-8542, Japan*
[2]*Faculty of Science, Department of Applied Physics, Fukuoka University, Fukuoka 814-0180, Japan*
[3]*Division of Theoretical Astronomy, National Astronomical Observatory of Japan, Tokyo 181-8588, Japan*
[4]*Department of Physics, Keio University, Yokohama 223-8522, Japan*

Macroscopic evolution of relativistic charged matter with chirality imbalance is described by the chiral magnetohydrodynamics (chiral MHD). One such astrophysical system is high-density lepton matter in core-collapse supernovae where the chirality imbalance of leptons is generated by the parity-violating weak processes. After developing the chiral MHD equations for this system, we perform numerical simulations for the real-time evolutions of magnetic and flow fields and study the properties of the chiral MHD turbulence. In particular, we observe the inverse cascade of the magnetic energy and the fluid kinetic energy. Our results suggest that the chiral effects that have been neglected so far can reverse the turbulent cascade direction from direct to inverse cascade, which would impact the magnetohydrodynamics evolution in the supernova core toward explosion.

I. INTRODUCTION

Relativistic matter with chirality imbalance (chiral matter, in short) is relevant to various physical systems from hot electroweak plasmas in the early Universe [1,2], quark-gluon plasmas created in heavy ion collision experiments [3], dense electromagnetic plasmas in neutron stars [4–7], and neutrino matter in core-collapse supernovae [8] to emergent chiral matter near band crossing points of Weyl (semi)metals [9–12]. In such chiral matter, anomalous transport phenomena that are absent in usual parity-invariant matter emerge. Two prominent examples are the current along the direction of a magnetic field, called the chiral magnetic effect (CME) [9,13–15], and the current along the direction of a vorticity, called the chiral vortical effect (CVE) [16–19]. Notably, the CME and CVE have close connection with the quantum violation of the chiral symmetry (or nonconservation of the chiral charge) in relativistic quantum field theories, known as the chiral anomaly [20,21]. The macroscopic evolution of charged chiral matter at a long time distance and long timescale is then described by the hydrodynamic theory by incorporating the effects of the chiral transport phenomena and the chiral anomaly. This is the *chiral magnetohydrodynamics* (chiral MHD) [8,22–26].

It is natural to expect that real-time evolution of chiral matter described by the chiral MHD is qualitatively different from that of nonchiral matter described by the conventional MHD. Analytically tractable regimes of the chiral MHD have been studied in Refs. [8,22–27]. Among others, inverse cascade of the fluid kinetic energy, i.e., the energy transfer from large to small scales, in addition to the inverse

cascade of the magnetic energy [28,29], in the chiral MHD turbulence was predicted for pure chiral matter under certain conditions [24]. This should be contrasted with the direct energy cascade (the energy transfer from small to large scales) in usual nonchiral matter. More recently, chiral MHD equations were numerically studied for high-temperature electroweak plasmas in the early Universe, and inverse energy cascade was indeed observed [30–32].[1] A possible realization of the chiral MHD turbulence in Weyl metals was also discussed [36].

One realization of chiral matter in astrophysical systems is the lepton matter in core-collapse supernovae, where the chirality imbalance of leptons is generated through the electron capture process that involves only left-handed leptons [6,8],

$$p + e_L^- \rightarrow n + \nu_L^e. \tag{1}$$

Although some of the chirality imbalance of electrons is erased by the finite electron mass [37,38], not all the imbalance is washed out. In particular, production of chirality imbalance is more effective as the temperature becomes higher [39] (see also Ref. [40] for another possible scenario). An alternative mechanism is that a fluid helicity generated by the CVE of the neutrinos *effectively* plays the role of the chirality imbalance of electrons and leads to the analog of CME for electrons even without such a chirality imbalance [8].

---

[1]The anomalous hydrodynamics with the CME in *external* electromagnetic fields has been studied in heavy ion physics [33–35].

083018-1

In this paper, we perform the three-dimensional (3D) numerical simulations of fully nonlinear chiral MHD equations for the high-density charged chiral matter at the core of a core-collapse supernova and study the properties of the chiral MHD turbulence. As a starting point of numerical simulations and for simplicity, we focus on the CME and chiral anomaly, but we ignore the CVE, fluid helicity, and cross-helicity as well as the contributions of the chiral transport in the neutrino matter in this paper. In this sense, our computations here should not be taken as a quantitative prediction. Rather, our motivation here is to show qualitatively new features due to the chiral effects that have been so far disregarded in the context of core-collapse supernovae. In fact, we observe the inverse cascade of the magnetic energy and the fluid kinetic energy due to the chiral effects in the high-density matter at the supernova core, similarly to the high-temperature electroweak plasmas in the early Universe.

This behavior is to be contrasted with conventional multidimensional neutrino radiation-hydrodynamic simulations for core-collapse supernovae (see Refs. [41,42] for reviews). In most of the 3D supernova models, the direct cascade of turbulent flows in the postshock region is dominant over the inverse cascade [42–44]. On the other hand, the dominance of the inverse cascade over the direct cascade (leading to a formation of large-scale flow) has been often observed in axisymmetric (2D) models. This large-scale flow may account for the vigor explosion found in the 2D models [41] though the detailed mechanism is under discussion [45]. The qualitative difference of our 3D turbulent behaviors from these previous results can be understood from the difference of the conservation laws between the two: while the conventional hydrodynamic theory respects the conservation of the energy alone, the chiral MHD respects the conservations of not only the energy but also a *nonzero helicity*.[2] Our results suggest that the chiral effects can reverse the turbulent cascade direction from direct to inverse cascade, which may be relevant to the mechanism of supernova explosions.

This paper is organized as follows. In Sec. II, we formulate the chiral MHD equations for protons and electrons with a chirality imbalance in the supernova core. In Sec. III, we provide the numerical results of the 3D chiral MHD turbulence. Sections IV and V are devoted to the discussion and conclusion, respectively. Throughout the paper, we use the units $\hbar = c = e = 1$ unless otherwise stated.

---

[2]In the case of 2D fluids, the conservation of *enstrophy*, in addition to the conservation of energy, leads to the inverse energy cascade [46]. Although the conservation of enstrophy is absent in three dimensions, the conservation of a nonzero helicity that is specific in three dimensions can lead to the inverse cascade, as we will explicitly show in this paper.

II. CHIRAL MHD IN THE SUPERNOVA CORE

A. Chiral MHD equations

Here, we generalize the conventional MHD by including the CME in the presence of a chirality imbalance of electrons generated by the process (1) in the supernova core. The chirality imbalance of electrons is characterized by the chiral chemical potential $\mu_A \equiv (\mu_R - \mu_L)/2$ (or the axial charge density n_A defined below), where $\mu_{R,L}$ is the chemical potential of the right- or left-handed electron. Alternatively, the fluid helicity produced by the CVE of neutrinos can be regarded as an effective chiral chemical potential μ_A. The precise value of μ_A (including the effective one) in the supernova core is determined by the microscopic process (1), the chirality flipping due to the finite electron mass [37], and nonlinear chiral MHD evolutions and is beyond the scope of the present paper. In this paper, we will treat n_A as a free parameter instead, and we will study the behaviors of the chiral MHD turbulence with nonzero n_A.

We start from relativistic continuity and momentum equations for the proton with the mass M and electron with the mass m (e.g., Ref. [47]),

$$\partial_t(\gamma_p \rho_p) + \boldsymbol{\nabla} \cdot (\rho_p \gamma_p \boldsymbol{v}_p) = 0, \tag{2}$$

$$\partial_t(\gamma_e \rho_e) + \boldsymbol{\nabla} \cdot (\rho_e \gamma_e \boldsymbol{v}_e) = 0, \tag{3}$$

$$\partial_t(\rho_p h_p \gamma_p^2 \boldsymbol{v}_p) + \boldsymbol{\nabla} \cdot (\rho_p h_p \gamma_p^2 \boldsymbol{v}_p \boldsymbol{v}_p)$$
$$= -\boldsymbol{\nabla}P_p + \gamma_p n_p \boldsymbol{E} + \boldsymbol{J}_p \times \boldsymbol{B} + \boldsymbol{F}_{pe}, \tag{4}$$

$$\partial_t(\rho_e h_e \gamma_e^2 \boldsymbol{v}_e) + \boldsymbol{\nabla} \cdot (\rho_e h_e \gamma_e^2 \boldsymbol{v}_e \boldsymbol{v}_e)$$
$$= -\boldsymbol{\nabla}P_e - \gamma_e n_e \boldsymbol{E} + \boldsymbol{J}_e \times \boldsymbol{B} + \boldsymbol{F}_{ep}, \tag{5}$$

where ρ is the mass density, v is the velocity, $\gamma = 1/\sqrt{1 - v^2}$ is the Lorentz factor, P is the pressure, $\boldsymbol{E}$ is the electric field, $\boldsymbol{B}$ is the magnetic field, $\boldsymbol{J}$ is the electric current density, and $h = 1 + P/\rho + \epsilon$ is the specific enthalpy with ϵ being the specific internal energy.[3] Subscripts "p" and "e" denote physical variables of protons and electrons, respectively. $\boldsymbol{F}_{pe}$ and $\boldsymbol{F}_{ep}$ represent the friction force between two fluid species and satisfy $\boldsymbol{F}_{pe} = -\boldsymbol{F}_{ep}$. The expressions of $\boldsymbol{J}_p$ and $\boldsymbol{J}_e$ are given by

$$\boldsymbol{J}_p = \gamma_p n_p \boldsymbol{v}_p, \tag{6}$$

$$\boldsymbol{J}_e = -\gamma_e n_e \boldsymbol{v}_e + \xi_B \boldsymbol{B}, \tag{7}$$

where n is the number density. The second term of the rhs in Eq. (7) is the CME, which arises due to the chirality imbalance of electrons.

---

[3]Note that the energy density ε is related to the specific internal energy ϵ via $\varepsilon = \rho(1 + \epsilon)$.

For a single right-handed electron with the chemical potential μ_R, the chiral magnetic conductivity ξ_B in the Landau frame reads [18,19,48],[4]

$$\xi_B = \frac{\mu_R}{4\pi^2}\left(1 - \frac{1}{2}\frac{n_R\mu_R}{\varepsilon + P}\right) - \frac{1}{24}\frac{n_R T^2}{\varepsilon + P} \simeq \frac{\mu_R}{8\pi^2}, \quad (8)$$

where n_R and ε are the charge and energy densities of right-handed electrons. In the last line, we used $\mu_R \gg T$ (expected in the supernova core) and the thermodynamic relation $\varepsilon + P \simeq \mu_R n_R$. In the system with right- and left-handed electrons, the equation above is modified to the form with replacing μ_R with $\mu_R - \mu_L$. Since the chemical potential is linked to the charge density via the relation $n_i = \mu_i^3/(6\pi^2)(i = R, L)$ for a noninteracting relativistic Fermi gas (which we assume for simplicity) with $\mu \gg T$,[5] the chiral magnetic conductivity is given by

$$\begin{aligned}\xi_B &= \frac{1}{8\pi^2}(\mu_R - \mu_L) \\ &= \frac{1}{8}\left(\frac{3}{\pi^4}\right)^{1/3}[(n_e + n_A)^{1/3} - (n_e - n_A)^{1/3}], \quad (9)\end{aligned}$$

where $n_A = n_R - n_L$ is the axial charge density and $n_e = n_R + n_L$ is the total charge density of electrons, which can be replaced approximately by ρ/M because of the charge neutrality ($n_e = n_p = \rho/M$) that we assume in our system.

In the following, we will derive one-fluid chiral MHD equations from two-fluid hydrodynamic equations for protons and electrons above. We assume that $|v_p| \ll 1$ and $|v_e| \ll 1$ and then use the nonrelativistic approximations $\gamma \approx 1$ and $h \approx 1$, which can be justified in the case of the supernova core.

First, we derive one-fluid continuity and momentum equations from Eqs. (2)–(7). As usual, the continuity equation is obtained from the sum of Eqs. (2) and (3) as

$$\partial_t\rho + \boldsymbol{\nabla} \cdot (\rho\boldsymbol{v}) = 0, \quad (10)$$

---

[4]We note that there is an ambiguity on the choice of the frame in relativistic hydrodynamics. In the frame where the CME takes the familiar form of the electric current, $\boldsymbol{j}_{CME} = \mu_R\boldsymbol{B}/(4\pi^2)$, the CME also contributes to the energy-momentum tensor, e.g., $T^{0i}_{CME} = T^{i0}_{CME} = \mu_R B^i/(8\pi^2)$ [18,19,48], which would change the momentum equation (15) below. (Such contributions seem to be missed in Refs. [30–32].) Following Ref. [8], we take here the Landau frame such that the CME contributes to $\boldsymbol{j}$, but not to $T^{\mu\nu}$.

[5]In general, the charge density of a noninteracting relativistic Fermi gas is given, as functions of the chemical potential and the temperature, by

$$n = \frac{\mu^3}{6\pi^2} + \frac{\mu T^2}{6}.$$

In the limit $\mu \gg T$, which is the regime of our interest, the first term on the rhs becomes dominant. In contrast, for $\mu \ll T$ relevant to the early Universe studied in Refs. [31,32], the second term mainly determines the charge density.

where the one-fluid mass density ρ and velocity $\boldsymbol{v}$ defined below can be approximated for $M \gg m$ by

$$\rho \equiv \rho_p + \rho_e = n(M + m) \simeq nM, \quad (11)$$

$$\boldsymbol{v} \equiv \frac{M\boldsymbol{v}_p + m\boldsymbol{v}_e}{M + m} \simeq \boldsymbol{v}_p. \quad (12)$$

The momentum equation is obtained from the sum of Eqs. (4) and (5) for $M \gg m$ and $M \gg mh_e$ by

$$\partial_t(\rho\boldsymbol{v}) + \boldsymbol{\nabla} \cdot (\rho\boldsymbol{v}\boldsymbol{v}) = -\boldsymbol{\nabla}P + \boldsymbol{J} \times \boldsymbol{B}. \quad (13)$$

where $P \equiv P_p + P_e$ is the total pressure and $\boldsymbol{J}$ is the total current density defined by

$$\begin{aligned}\boldsymbol{J} &\equiv \boldsymbol{J}_p + \boldsymbol{J}_e \\ &= [n(\boldsymbol{v}_p - \boldsymbol{v}_e)] + [\xi_B\boldsymbol{B}] = \boldsymbol{J}_{MHD} + \boldsymbol{J}_{CME}, \quad (14)\end{aligned}$$

where $\boldsymbol{J}_{MHD}$ is the current density due to the velocity difference between positive and negative charges and $\boldsymbol{J}_{CME}$ is that due to the CME. By adding the viscous term in Eq. (13) as usual (see, e.g., Refs. [49,50]), we obtain

$$\rho\mathcal{D}_t\boldsymbol{v} = -\boldsymbol{\nabla}P + \boldsymbol{J} \times \boldsymbol{B} + \boldsymbol{\nabla} \cdot \boldsymbol{\Pi}, \quad (15)$$

where $\mathcal{D}_t$ is the Lagrangian time derivative and $\Pi_{ij} = 2\rho\nu S_{ij}$ is the viscous stress tensor with the viscosity ν and the strain rate tensor,

$$S_{ij} = \frac{1}{2}\left(\partial_j v_i + \partial_i v_j - \frac{2}{3}\delta_{ij}\partial_i v_i\right). \quad (16)$$

The bulk viscosity is neglected for simplicity in this study.

Let us next derive Ohm's law and the resulting energy and induction equations. Multiplying Eq. (4) by m/ρ and Eq. (5) by M/ρ and taking their difference, we have

$$\begin{aligned}mD_t\left(\frac{\boldsymbol{J}_{MHD}}{n}\right) &+ \frac{1}{\rho}(m\boldsymbol{\nabla}P_p - M\boldsymbol{\nabla}P_e) \\ &= \boldsymbol{E} + \frac{1}{\rho}(m\boldsymbol{J}_p - M\boldsymbol{J}_e) \times \boldsymbol{B} - \eta\boldsymbol{J}_{MHD}, \quad (17)\end{aligned}$$

where η is the resistivity and the canonical relation of $\boldsymbol{F}_{ep} = \eta n\boldsymbol{J}_{MHD}$ is used. The second term of the rhs is rewritten by

$$\frac{1}{\rho}(m\boldsymbol{J}_p - M\boldsymbol{J}_e) \times \boldsymbol{B} = \left(\boldsymbol{v} - \frac{M - m}{\rho}\boldsymbol{J}_{MHD} - \frac{M}{\rho}\boldsymbol{J}_{CME}\right) \times \boldsymbol{B}. \quad (18)$$

For $M \gg m$ and for a sufficiently long timescale $t \gg 1/\omega_{pe}$ with ω_{pe} being the plasma frequency of electrons, Eq. (17) becomes

$$E + v \times B - \eta J_{\text{MHD}} = \frac{1}{n} J \times B - \frac{1}{n} \nabla P_e, \quad (19)$$

where the first and second terms on the rhs are the Hall term and the electron pressure term, respectively. In Eq. (19), we neglect the electron inertia and the proton pressure by focusing on lower-frequency motions of the plasma than the electron plasma oscillation due to the local charge separation. This is an essential difference between our one-fluid chiral MHD system and the original two-fluid description of the chiral plasma. When ignoring the terms on the rhs for simplicity, the modified Ohm's law including the CME becomes

$$E + v \times B = \eta(J - J_{\text{CME}}). \quad (20)$$

Note that the Joule-heating term in the internal energy equation can be evaluated from Eq. (20) by $J \cdot E$. Hence, the energy equation is given by

$$\rho \mathcal{D}_t \epsilon = -P \nabla \cdot v + 2\rho \nu S^2 + \eta J \cdot (J - J_{\text{CME}}). \quad (21)$$

Furthermore, from Faraday's law $\partial_t B = -\nabla \times E$, the induction equation modified by the CME is obtained as

$$\partial_t B = \nabla \times (v \times B) + \eta \nabla^2 B + \eta \nabla \times (\xi_B B). \quad (22)$$

Here, Ampère's law $J = \nabla \times B$ is used. The last term on the rhs is the correction due to the CME.

Finally, the time evolution of n_A is given by the chiral anomaly equation [20,21],

$$\partial_\mu J_A^\mu = \frac{1}{2\pi^2} E \cdot B, \quad (23)$$

where J_A^μ is the axial 4-current. Using Eq. (19), this can be rewritten as

$$\partial_t n_A = \frac{\eta}{2\pi^2}(J - J_{\text{CME}}) \cdot B, \quad (24)$$

where, for our step-by-step strategy, we ignore the advection term, the diffusion term, the so-called chiral separation effect (CSE) [51,52], $J_{\text{CSE}}^A = \xi_B^A B$ with ξ_B^A being the transport coefficient, and the cross-helicity $J_{\text{CSE}}^{A0} = \xi_B^A v \cdot B$, for simplicity. Note that, under this simplification, Eq. (24) can be understood as the conservation of helicity (fermion helicity plus magnetic helicity, but without cross-helicity and fluid helicity) [8]; see also the remark below.

For an equation of state (EOS), we adopt the ideal gas law,

$$P = (\Gamma - 1)\rho \epsilon, \quad (25)$$

for simplicity, where $\Gamma = 5/3$ in the adiabatic index. Then, we can close the system. The set of Eqs. (9), (10), (15),

(21), (22), and (24) coupled with the EOS (25) is solved simultaneously in our simulation.

Before proceeding further, we comment on several simplifications of our formulation in this paper. Here and below, we focus on the CME and chiral anomaly, but for simplicity, we ignore the CVE, $J_{\text{CVE}} = \xi_\omega \omega$, the CSE expressed by $J_{\text{CSE}}^A = \xi_B^A B + \xi_\omega^A \omega$, and the other types of helicity (fluid helicity and cross-helicity). Here, $\omega \equiv \nabla \times v$ is the fluid vorticity, and ξ_ω is the chiral vortical conductivity. In particular, we ignore the contributions of the chiral effects of neutrinos. Incorporating the CVE and CSE is necessary to ensure the conservation of total helicity (summation of the fermion helicity, magnetic helicity, fluid helicity, and cross-helicity), which would be an important question to be studied in the future; see Refs. [8,53] for such a generic conservation law of helicity. The importance of the CVE in the chiral MHD turbulence will briefly be discussed in Sec. IV B.

B. Chiral plasma instability

To build up the simulation model, we should bear in mind the driving mechanism of the chiral MHD turbulence. The presence of the CME induces the amplification of the magnetic field due to the chiral plasma instability (CPI); see, e.g., Refs. [5,6,8] in the context of neutron stars and supernovae. By inserting the perturbation $\delta B \propto \exp(ik \cdot x + \sigma t)$ into the induction equation (22) around the stationary uniform background $v = B = 0$, we obtain the dispersion equation for the CPI,

$$\sigma = \eta \xi_B k - \eta k^2, \quad (26)$$

where $k = |k|$ is the wave number. Shown by the solid line in Fig. 1(a) is the real part of $\sigma = \sigma(k)$ that characterizes the growth rate of the CPI. The dashed line denotes the linear dispersion relation neglecting the k^2 term in Eq. (26). The vertical and horizontal axes are normalized by the maximum growth rate $\sigma_{\text{max}} = \eta \xi_B^2/4$ and ξ_B, respectively. The CPI grows only in the low–wave number regime,

$$k < k_{\text{crit}} = \xi_B, \quad (27)$$

and becomes maximum when $k = \xi_B/2$, indicating that the onset of the CPI is due solely to the presence of the chirality imbalance. While the growth rate of the CPI becomes larger with the increase of η, the magnetic diffusion term plays a role in, as usual, suppressing the modes in the high–wave number regime $k > k_{\text{crit}}$ (see the dashed line). The typical wavelength of the CPI becomes longer with the decrease of ξ_B, suggesting the tendency toward inverse energy cascade under the situation in which ξ_B decreases as a function of time.

It is worth noting here that the CME is somewhat similar to the α effect in the mean-field dynamo theory [54–56]. When dividing the variables of the induction equation into the ensemble-averaged values and fluctuating components, the α effect appears in the turbulent electromotive force as
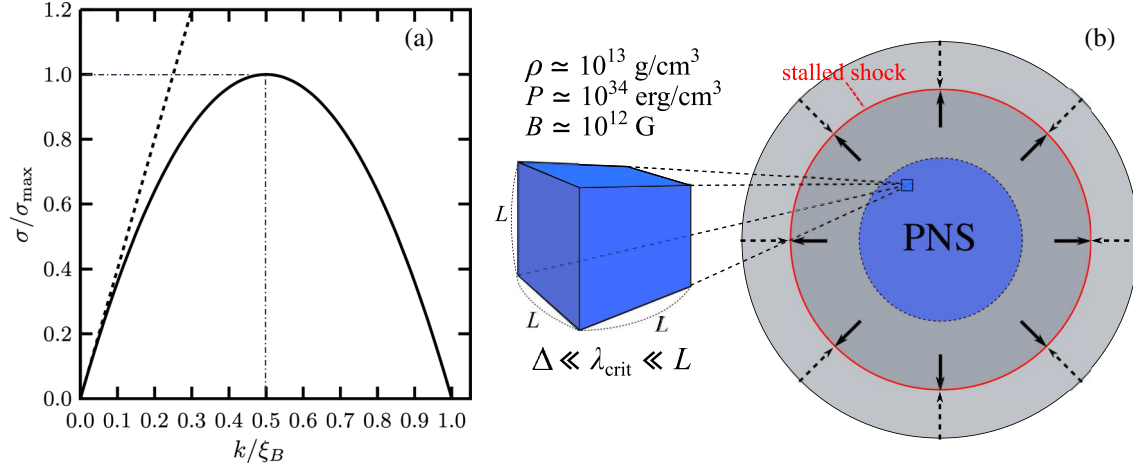
FIG. 1. (a) Dispersion relation of the CPI. (b) Setup for our local box simulation. The global structure of the supernova core (right) and extracted local Cartesian patch (left). The box size L is chosen so as to resolve $\lambda_{\rm crit}$.

an induction term. It is a consequence of the forced symmetry breaking in rotating astrophysical bodies, such as the Sun, stars, and accretion disks, and has been widely studied as an origin of the large-scale magnetic field commonly observed in these objects [57–60]. On the other hand, the CME is a pure quantum effect that originates from the explicit parity symmetry breaking by the chirality of fermions. Although one can expect common traits in the macroscopic hydrodynamic evolutions between them (see Refs. [25,31,32,61] for the chiral MHD turbulence in the early Universe), there is also a difference: the total helicity is vanishing for the α effect in the nonchiral matter, whereas this is not the case in chiral matter. In particular, a nonzero magnetic helicity can be generated *globally* in chiral matter.

III. NUMERICAL RESULTS

A. Simulation setup

We perform a series of 3D simulations by adopting a local Cartesian model, which zooms in on a small patch of the proto-neutron star (PNS), with the cubic periodic box. See Fig. 1(b) for the schematic view of our numerical model. In most of our simulations, the size of the simulation domain L and the grid size $\Delta \equiv L/N$ (N is the number of numerical grids) are determined so as to resolve the critical wavelength of the CPI defined by $\lambda_{\rm crit} \equiv 2\pi/\xi_B$, that is,

$$\Delta \ll \lambda_{\rm crit} \ll L. \qquad (28)$$

We will discuss how the resolution and the box size of the simulation model affect the behaviors of the chiral MHD turbulence in Secs. III C and III E.

The MHD equations are solved by the second-order Godunov-type finite-difference scheme that employs an approximate MHD Riemann solver [62,63]. The magnetic field evolves with the consistent method of characteristics-constrained transport (MoC-CT) scheme with including the CME as a part of the electromotive force (see Refs. [64,65] for the MoC-CT method). The chirality imbalance is updated according to Eq. (24) straightwardly with the MHD variables.

All the numerical models have the same initial density and pressure of $\rho = 5.0$ and $P = 1.0$ in the unit of 100 MeV $= 1$, which are equivalent to $\rho \simeq 10^{13}$ g/cm^3 and $P \simeq 10^{34}$ erg/cm^3 of the typical PNS (see, e.g., Ref. [66]). For the fiducial run, we adopt the uniform axial charge density $n_A = 0.1$ $(\equiv n_{A0})$, which corresponds to $\xi_B = 4.2 \times 10^{-3}$ $(\equiv \xi_{B0})$, the uniform viscosity $\nu = 0.1$ $(\equiv \nu_0)$, the uniform resistivity $\eta = 100.0$ $(\equiv \eta_0)$, and a resolution of $N^3 = 256^3$ grid points. Since $\lambda_{\rm crit}$ for these values of the parameters is estimated as $\lambda_{\rm crit} = 1.5 \times 10^3$, we choose $L = 2 \times 10^4$ $(\equiv L_0)$ to satisfy the condition (28).

As stated in Sec. I, a few physical processes are relevant for the origin of the finite axial charge density n_A. One scenario is the chiral imbalance produced by the electron capture process (1) before the neutrino trapping $(\rho_c \lesssim 10^{12}$ g/cm^3 with ρ_c the central density of stars). After the neutrino trapping, the electron capture process slowly proceeds since the inverse process blocks the production of the imbalance and diffusion process of the neutrino controls the net rate. In an alternative scenario, the fluid helicity of the trapped neutrino also plays the role of n_A. This fluid helicity could be induced by the rotation or the convection of the star. In this study, we change n_A parametrically since we cannot treat these effects in a self-consistent manner that requires a global neutrino radiation-hydrodynamics simulation.

The resistivity η of moderately degenerate electrons is expected to be of the order of 0.1–1.0 (under the scaling of 100 MeV $= 1$) in the PNS (see, e.g., Ref. [67]). Since η chosen in our fiducial model is larger than the actual value, the dependence of the chiral MHD turbulence on η is

TABLE I. Summary of the simulation runs. Two diagnostic quantities B_{sat} and $\xi_{B,sat}$ are defined by $B_{sat} \equiv \langle \boldsymbol{B}^2(t_{sat}) \rangle^{1/2}$ and $\xi_{B,sat} \equiv \langle \xi_B(t_{sat}) \rangle$, where t_{sat} is the time when the system reaches saturation. See the text for further explanations.

	N^3	η	L	n_A	$\xi_{B,ini}$	τ_{CPI}	B_{sat}	$\xi_{B,sat}/\xi_{B,ini}$
Model 1	256^3	100.0	2×10^4	0.1	4.2×10^{-3}	2.3×10^3	2.5×10^{-2}	0.077
Model 2	128^3	100.0	2×10^4	0.1	4.2×10^{-3}	2.3×10^3	2.3×10^{-2}	0.075
Model 3	64^3	100.0	2×10^4	0.1	4.2×10^{-3}	2.3×10^3	1.4×10^{-2}	0.077
Model 4	128^3	10.0	2×10^4	0.1	4.2×10^{-3}	2.3×10^4	2.5×10^{-2}	0.078
Model 5	128^3	1.0	2×10^4	0.1	4.2×10^{-3}	2.3×10^5	2.7×10^{-2}	0.077
Model 6	128^3	1.0	1×10^5	0.1	4.2×10^{-3}	2.3×10^5	1.1×10^{-2}	0.024
Model 7	64^3	1.0	1×10^4	0.1	4.2×10^{-3}	2.3×10^5	3.6×10^{-2}	0.15
Model 8	32^3	1.0	4×10^3	0.1	4.2×10^{-3}	2.3×10^5	4.9×10^{-2}	0.39
Model 9	128^3	1.0	4×10^3	0.416	2.1×10^{-2}	9.2×10^3	1.2×10^{-1}	0.075
Model 10	128^3	1.0	1×10^5	0.020	8.4×10^{-4}	5.7×10^6	5.5×10^{-3}	0.078

studied in Sec. III D. In contrast, the viscosity ν due to electrons is expected to be $\mathcal{O}(10^{-2})$ and is compatible with the value chosen in the fiducial run. The dependence of the chiral MHD turbulence on the magnetic Prandtl number ($\equiv \nu/\eta$) is beyond the scope of this study but a target of our future work.

In addition to the fiducial run, we simulate a number of models with varying model parameters, such as N, η, L, and n_A, to study their impacts on the chiral MHD turbulence. The parameters adopted in our simulation models are listed in Table I with a few diagnostic quantities. A random small "seed" magnetic field with the amplitude $|\delta \boldsymbol{B}| < 0.01$, which gives the maximum value $\simeq 10^{12}$ G in the cgs unit, is introduced into the initial stationary state with $|\boldsymbol{v}| = 0.0$.

B. Fiducial run

The basic property in the evolution and saturation of the chiral MHD turbulence is illustrated with the fiducial model (model 1) as an example. We first define the strength of the mean magnetic field by

$$\langle B^2 \rangle^{1/2} \equiv \left(\frac{1}{V} \int B^2 \mathrm{d}^3 \boldsymbol{x} \right)^{1/2}, \qquad V \equiv \int \mathrm{d}^3 \boldsymbol{x}, \quad (29)$$

where $B \equiv |\boldsymbol{B}|$ is the magnitude of the magnetic field and the angular brackets denote the volume average. Similarly, the mean magnetic and kinetic energies are defined by

$$\epsilon_M \equiv \frac{1}{4\pi} \langle B^2 \rangle, \qquad \epsilon_K \equiv \frac{1}{2} \langle \rho v^2 \rangle, \quad (30)$$

respectively, where $v \equiv |\boldsymbol{v}|$ is the magnitude of the flow velocity. Figure 2(a) shows the temporal evolution of $\langle B^2 \rangle^{1/2}$ at the early evolutionary stage. In addition, the evolutions of ϵ_M (red solid) and ϵ_K (blue dashed) are also depicted in Fig. 2(b). The horizontal axes are normalized by the growth time of the most growing mode of the CPI defined by

$$\tau_{CPI} \equiv \sigma_{max}^{-1} = 4(\eta \xi_{B,ini}^2)^{-1}, \quad (31)$$

where $\xi_{B,ini}$ is the initial value of ξ_B. For the fiducial model, τ_{CPI} is evaluated as 2.3×10^3. The dashed line in the panel (a) is a reference slope proportional to $\exp(\sigma_{max} t)$.

As seen in Fig. 2(a), the early evolution of $\langle B^2 \rangle^{1/2}$ agrees with the linear analysis of the CPI. During this stage, the magnetic field is amplified by a factor of $\mathcal{O}(10^4)$. After the early exponential growth, it enters the nonlinear stage at $t \simeq 20\tau_{CPI}$. We emphasize that the saturation amplitude and amplification factor of the magnetic field do *not* depend on the strength of the initial magnetic field but on the initial
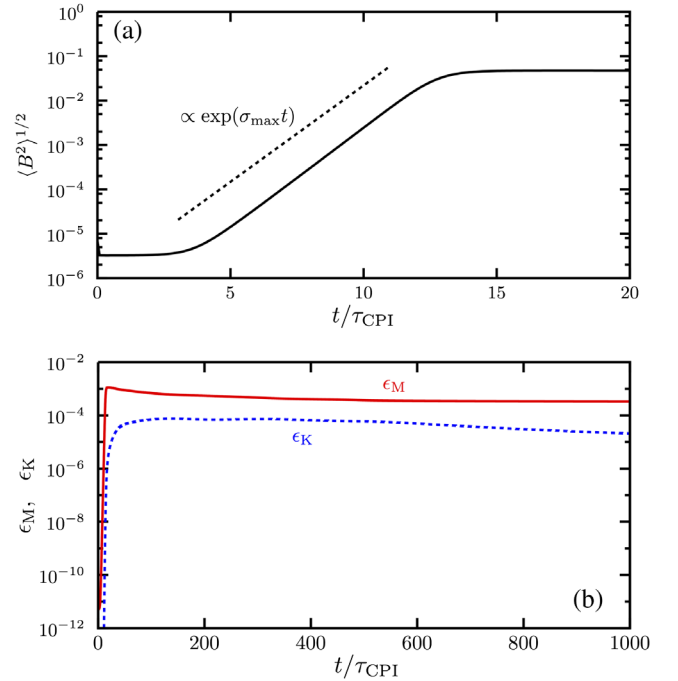

FIG. 2. Temporal evolutions of $\langle B^2 \rangle^{1/2}$ at the early exponential-growth stage [panel (a)] and ϵ_M (red solid) and ϵ_K (blue dashed) [panel (b)] for the fiducial run.
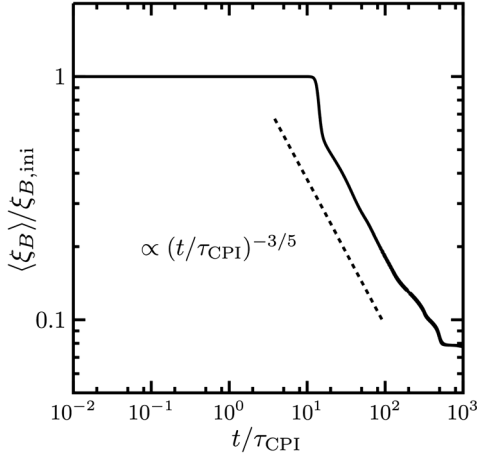
FIG. 3. Temporal evolution of $\langle \xi_B \rangle$ normalized by $\xi_{B,\text{ini}}$. The dashed line is a reference slope proportional to $(t/\tau_{\text{CPI}})^{-3/5}$.

chirality imbalance (see Sec. III E). Hence, the magnetic field can be amplified to the same level as long as we use the same ξ_B as that of the fiducial model, even if a weaker initial magnetic field is applied.

The frozen-in property between the plasma and the magnetic field causes the coevolution of the flow field. As shown in Fig. 2(b), ϵ_K rapidly grows when $t \lesssim 100\tau_{\text{CPI}}$ and then reaches a saturation amplitude an order of magnitude smaller than ϵ_M. When $t \gtrsim 200\tau_{\text{CPI}}$, ϵ_K gradually decreases probably due to the viscous dissipation of the small-scale structure of the flow field. For example, the viscous timescale of the flow structure with the size $l \simeq L/100$ can be evaluated as $\tau_{\text{vis}} = l^2/\nu \simeq 200\tau_{\text{CPI}}$.

Since the chiral MHD turbulence is sustained by the energy conversion from the chirality imbalance to the magnetic energy, $\langle \xi_B \rangle$ decreases with the increase of the magnetic energy. Shown in Fig. 3 is the temporal evolution of $\langle \xi_B \rangle$ normalized by $\xi_{B,\text{ini}}$. After the rapid drop stage, it decreases gradually in proportion to $(t/\tau_{\text{CPI}})^{-3/5}$ and finally reaches saturation at $t = t_{\text{sat}} \simeq 10^3 \tau_{\text{CPI}}$ with the floor value $\xi_{B,\text{sat}} \equiv \langle \xi_B(t_{\text{sat}}) \rangle \simeq 0.077 \xi_{B,\text{ini}}$.

As will be examined in Sec. III E in detail, the floor value $\xi_{B,\text{sat}}$ is definitely influenced by L. Using the value of $\xi_{B,\text{sat}}$ in Table I, λ_{crit} of the CPI at the saturated stage ($t \simeq 10^3 \tau_{\text{CPI}}$) is evaluated as

$$\lambda_{\text{crit}} = \frac{2\pi}{\xi_{B,\text{sat}}} \simeq 2.0 \times 10^4 = L_0, \qquad (32)$$

suggesting that the energy conversion from the chirality imbalance into the magnetic energy is terminated when ξ_B is reduced to the value at which the unstable wavelength of the CPI becomes comparable to the size of the calculation domain.

As expected from the temporal behavior of $\langle \xi_B \rangle$, the spatial structures of $\mathbf{B}$ and $\mathbf{v}$ exhibit the inverse energy cascade. Series of snapshots of the distributions of B_x

and v_x at different times on the x–y cutting plane at $z = 0$ are shown in Figs. 4 and 5. The red and blue tones depict the positive and negative values of the fields. The vertical and horizontal axes are normalized by $L/2$. While B_x and v_x have small-scale structures in the early evolutionary stage [panels (a)–(f)], they evolve as time passes to organize the large-scale structure with the spatial scale comparable to the size of the calculation domain [panels (g)–(i)]. It should be stressed that, since there is no specific direction in our simulation, not only the x component but also the y and z components of $\mathbf{B}$ and $\mathbf{v}$ also have similar large-scale structures; see Fig. 6 for the 3D structures of $\mathbf{B}$ and $\mathbf{v}$, in which their magnitudes at the early and fully nonlinear stages are visualized.

The inverse-cascade process of the chiral MHD turbulence can be seen in the temporal evolution of the 3D spectrum of the magnetic energy density $\epsilon_M(k)$ as shown in Fig. 7(a). Here, $\epsilon_M(k)$ is defined by

$$\epsilon_M(k) \equiv \frac{1}{2} \sum_{k_x,k_y,k_z} \hat{\mathbf{B}}(\mathbf{k}) \cdot \hat{\mathbf{B}}^*(\mathbf{k}), \qquad (33)$$

where $\hat{\mathbf{B}}(\mathbf{k})$ is the 3D Fourier transform of $\mathbf{B}(\mathbf{x})$ with $\hat{\mathbf{B}}^*(\mathbf{k})$ being its complex conjugate and the summation is over all k_x, k_y, and k_z such that $k_x^2 + k_y^2 + k_z^2 = k^2$. The blue and red curves correspond to the initial and nonlinear states (at $t \simeq \tau_{\text{CPI}}$ and $t \simeq 290\tau_{\text{CPI}}$). The gray lines are the spectra at the time between these two states. In Fig. 7(b), not only $\epsilon_M(k)$ (red) but also the spectrum of the kinetic energy density $\epsilon_K(k)$ (blue), which is calculated in a similar manner as Eq. (33), at the fully nonlinear stage ($t \simeq 500\tau_{\text{CPI}}$) are shown. The horizontal axes are normalized by $k_L = 2\pi/L$ in both panels.

$\epsilon_M(k)$ begins to grow for $k \lesssim k_{\text{crit}}$, which is the linearly unstable regime of the CPI, and thus it is the energy injection scale for the chiral MHD turbulence. While the magnetic energy is dominantly contained in the low–wave number modes, it is transferred to the smaller-scale structure via the direct cascade process. A similar evolution history can also be seen in $\epsilon_K(k)$, despite a remarkable difference in the spectral slopes, roughly $\epsilon_M(k) \propto k^{-3}$ and $\epsilon_K(k) \propto k^{-2}$ in the low-k regime. Not only the spatial distribution of the field structures in Figs. 4–6 but also the spectra in Fig. 7 indicate that a more prominent large-scale structure develops in the magnetic field than in the velocity field.

C. Dependence on resolution

To conduct the parametric study, we need to know how many grids are required at least to correctly capture the behavior of the chiral MHD turbulence. The convergence is checked by comparing the models with different resolutions. Models 2 and 3 have the number of grids $N^3 = 128^3$ and $N^3 = 64^3$ with keeping the other parameters the same as in the fiducial model with $N^3 = 256^3$ (model 1).
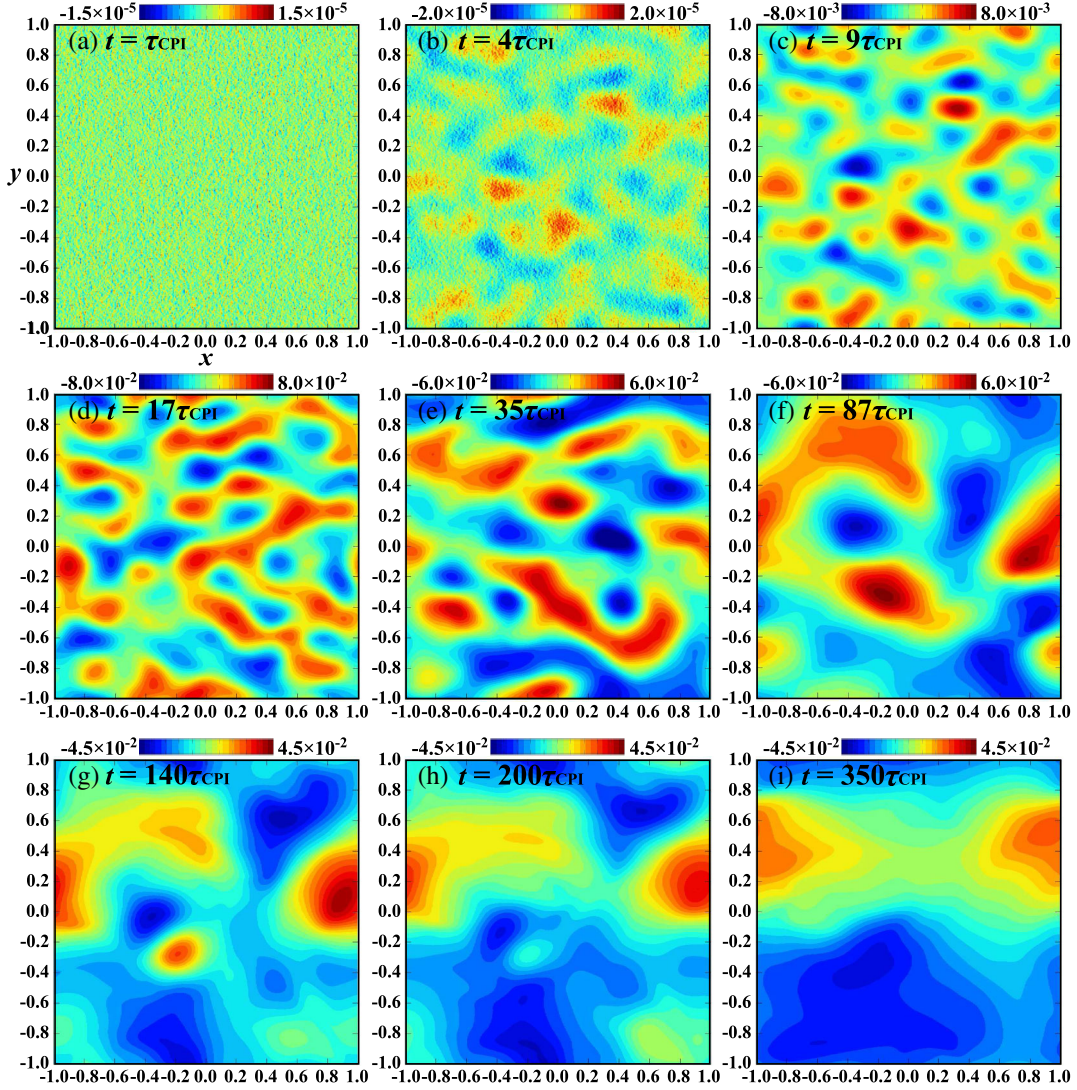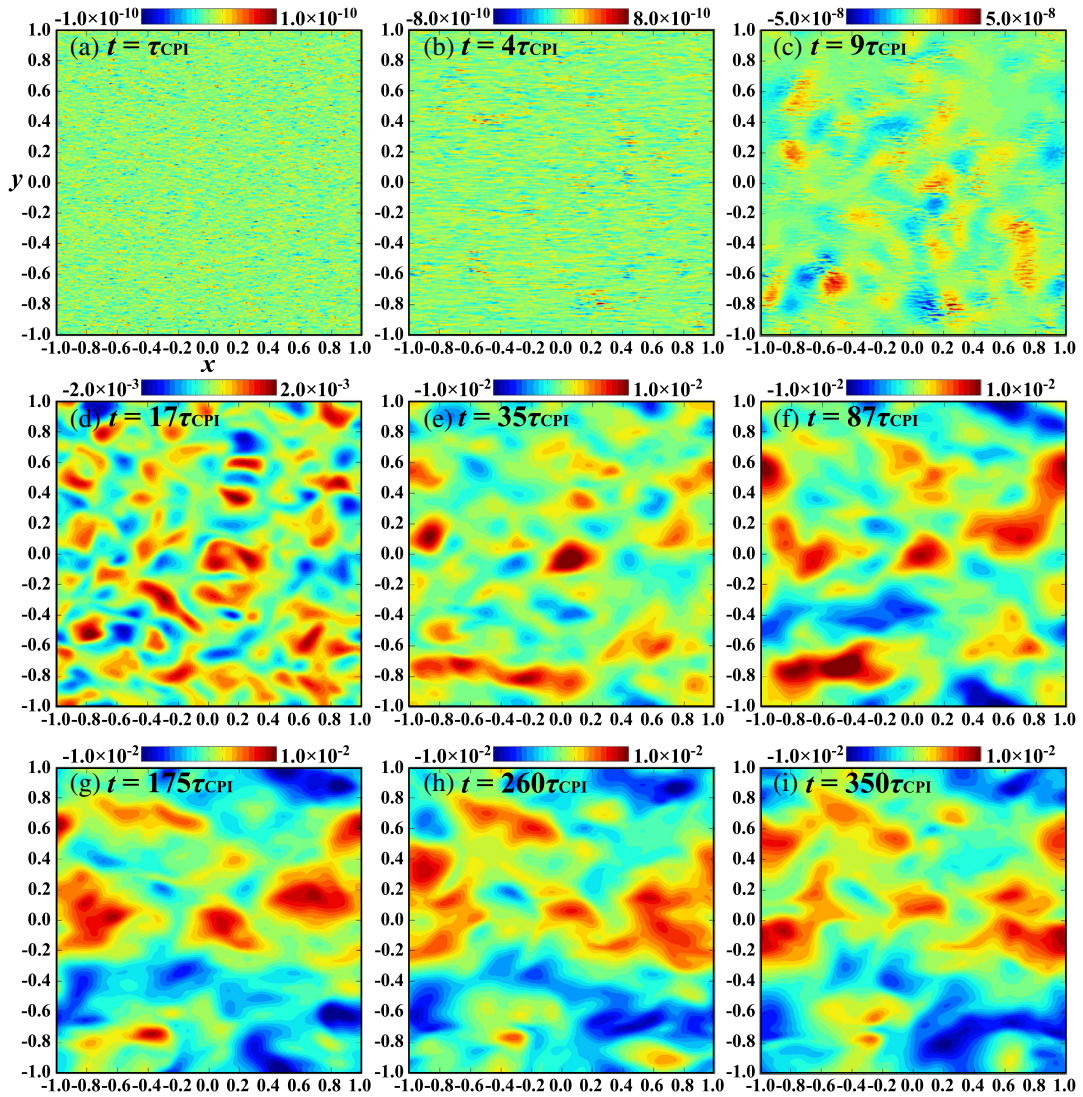
FIG. 4.   A series of snapshots of the distribution of B_x on the x–y cutting plane at $z = 0$. The vertical and horizontal axes are both normalized by $L/2$.

Figure 8 shows the temporal evolution of (a) ϵ_M and (b) $\langle \xi_B \rangle$ for the models with different resolutions. The red, blue, and green lines denote models 1–3, respectively, in both panels. We find that the saturation amplitude of ϵ_M converges when $N \gtrsim 128$. Model 3 has an insufficient resolution, yielding the lower saturation amplitude. In contrast, $\xi_{B,\mathrm{sat}}$ is not affected by the resolution, suggesting again that it is determined numerically by the size of the calculation domain.

The convergence of the numerical result can be confirmed more quantitatively by comparing the spectra of the models. Shown in Fig. 9(a) is $\epsilon_M(k)$ at the saturated stage for the models with different resolutions. The red, blue, and green lines correspond to models 1–3, respectively. Models 1 and 2 with $N^3 = 256^3$ and 128^3 have almost the same spectral profiles and amplitudes. However, the spectrum of the model 3 with $N^3 = 64^3$ deviates significantly from

them, verifying that it is insufficient for correctly capturing the chiral MHD turbulence.

The distributions of B_x at the saturated stage on the x–y cutting plane at $z = 0$ for the models 1–3 are presented in Figs. 9(b)–9(d). The red and blue tones depict the positive and negative values of the magnetic field. While the large-scale magnetic structure with the wavelength comparable to the box size is a common outcome of the nonlinear evolution of the chiral MHD turbulence as a result of the inverse cascade, the strength of the magnetic field is an order of magnitude weaker in the lowest resolution model (model 3) than in the sufficiently resolved models (models 1 and 2).

From these results, the convergence seems to be achieved when

$$\lambda_{\mathrm{CPI}}/\Delta \gtrsim 7. \tag{34}$$

FIG. 5.   A series of snapshots of the distribution of v_x on the x–y cutting plane at $z = 0$. The vertical and horizontal axes are both normalized by $L/2$.

At the same time, our results imply that even lower resolution calculation is acceptable as long as we are only interested in $\xi_{B,\mathrm{sat}}$.

D. Dependence on resistivity

One of the key parameters for the CPI and its driven MHD turbulence is the resistivity η. As described in Fig. 1(a), one of the interesting features of the CPI is that its linear growth rate becomes higher with the increase of η, while it suppresses the MHD turbulence in most cases of the conventional nonchiral MHD. The effects of η on the nonlinear behavior of the chiral MHD turbulence is of our interest here. We run the models 4 and 5 with $\eta = 10$ and 1 and then compare them with the model 2 with $\eta = 100$. We take the resolution and the other parameters to be the same.

In Fig. 10, we show the temporal evolution of ϵ_M for the models with $\eta = 1$ (red), 10 (blue), and 100 (green),

respectively. The difference between panels (a) and (b) is the normalization unit of time. In panel (a), the simulation time of each model is normalized in common by τ_{CPI} for the model with $\eta = \eta_0$, $\tau_{\mathrm{CPI},f} \equiv 4(\eta_0 \xi_{B,\mathrm{ini}}^2)^{-1}$. In contrast, in panel (b), it is normalized by τ_{CPI} evaluated with η of each model.

As seen in panel (a), the actual growth time of the chiral MHD turbulence becomes shorter with increasing η, which is consistent with the linear analysis of the CPI [see Eq. (26)]. However, when normalizing the simulation time by τ_{CPI} of each model, the evolution history until the nonlinear stage is identical between the models. In addition, the saturation amplitude of ϵ_M is also roughly the same between the models in spite of the difference of η.

The independence of the nonlinear behavior of the chiral MHD turbulence on η can be seen even in the comparison of the spectra. Shown in Fig. 11 is $\epsilon_M(k)$ at the saturated
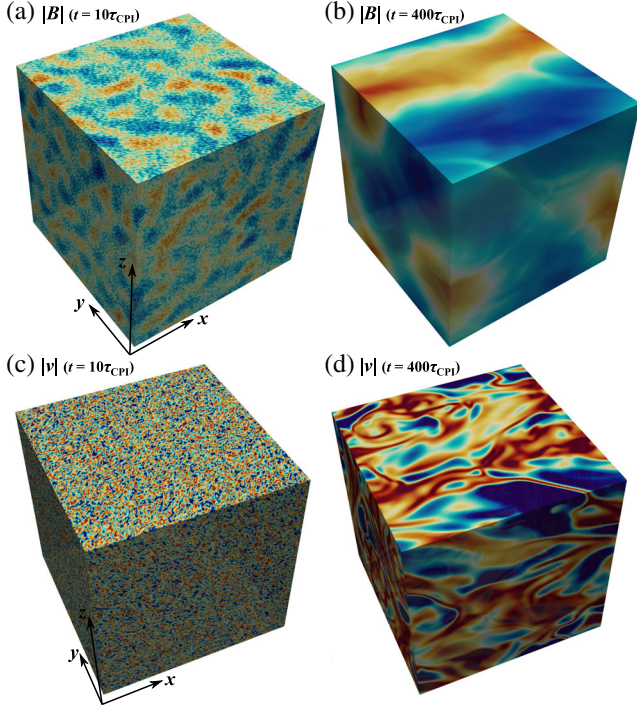
FIG. 6.   3D visualization of B [panels (a) and (b)] and v [panels (c) and (d)] at the early evolutionary stage ($t = 10\tau_{\mathrm{CPI}}$) and fully nonlinear stage ($t = 400\tau_{\mathrm{CPI}}$), respectively. The red and blue tones denote the lower and higher magnitudes of the fields.

stages for these models. The red, blue, and green lines denote the models with $\eta = 1$, 10 and 100, respectively. Regardless of the size of η, the chiral MHD turbulence exhibits a similar spectral property. All the results suggest that η does not have a strong impact on the nonlinear behavior of the chiral MHD turbulence though it changes the linear growth rate of the CPI.

The evolution history of $\langle \xi_B \rangle$ might be one of the few differences between these models. The temporal evolutions

of ξ_B for these models are shown in Fig. 12. Three dashed lines are the reference slopes proportional to $(t/\tau_{\mathrm{CPI}})^{-3/5}$, $(t/\tau_{\mathrm{CPI}})^{-6/5}$, and $(t/\tau_{\mathrm{CPI}})^{-3}$, respectively. While $\xi_{B,\mathrm{sat}}$ is almost the same, t_{sat} is difference between them. With decreasing η, the normalized time required for the saturation becomes shorter. This might be because the higher magnetic diffusion makes the magnetic structure harder to grow at the nonlinear stage.

E. Dependence on box size

As discussed in Sec. III B, $\xi_{B,\mathrm{sat}}$, which is responsible for the conversion efficiency of the chirality imbalance into the magnetic energy, is expected to be determined by the size of the calculation domain in our local-box model. To verify this, we examine the response of the chiral MHD turbulence to the change of L. The models with $L = 5L_0, L_0/2$, and $L_0/5$ (models 6, 7, and 8) are compared with model 5 with $L = L_0$. We keep, as far as possible, the ratio $\lambda_{\mathrm{CPI}}/\Delta$ constant rather than the number of grids, except for the largest box model with $L = 5L_0$ (model 6) in which case the higher resolution of $N^3 = 640^3$ is required. As was shown in Sec. III C, the insufficient resolution does not matter as long as we focus on $\xi_{B,\mathrm{sat}}$. The other physical parameters are kept unchanged from model 5 with the fiducial box size.

Shown in Fig. 13 is the temporal evolution of $\langle \xi_B \rangle$ for each model until the saturation. The orange, red, green, and blue lines are for the models with $L = 5L_0, L_0, L_0/2$, and $L_0/5$, respectively. The distributions of B_x on the x–y cutting plane at $z = 0$ at the saturated stage are also demonstrated for each model in Fig. 14. The axes of all the panels are normalized by $L_0/2$ of the fiducial model.

We find that $\xi_{B,\mathrm{sat}}$ is different when L is varied, despite the same physical parameters except for L. It is inversely correlated with L, i.e., $\xi_{B,\mathrm{sat}} \propto L^{-1}$ (see Table I), and
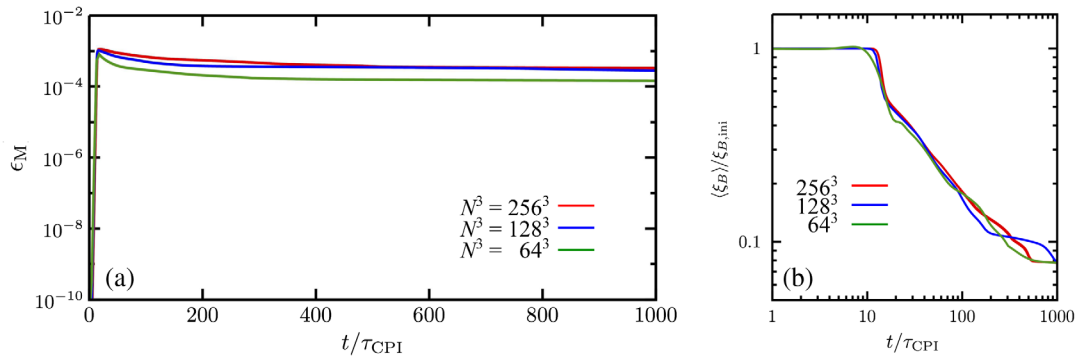

FIG. 7.   (a) Temporal evolution of $\epsilon_{\mathrm{M}}(k)$. The blue and red curves denote the initial state at $t = \tau_{\mathrm{CPI}}$ and nonlinear state at $t = 290\tau_{\mathrm{CPI}}$. The gray curves are the states between them. (b) $\epsilon_{\mathrm{M}}(k)$ (red) and $\epsilon_{\mathrm{K}}(k)$ (blue) at the saturated state ($t = 500\tau_{\mathrm{CPI}}$). The dashed lines are reference slopes proportional to k^{-3} and k^{-2}.

FIG. 8.   Temporal evolutions of (a) ϵ_M and (b) $\langle \xi_B \rangle$ for the models with different numerical resolutions. The red, blue, and green lines are for the models with $N = 256^3$, 128^3, and 64^3, respectively.
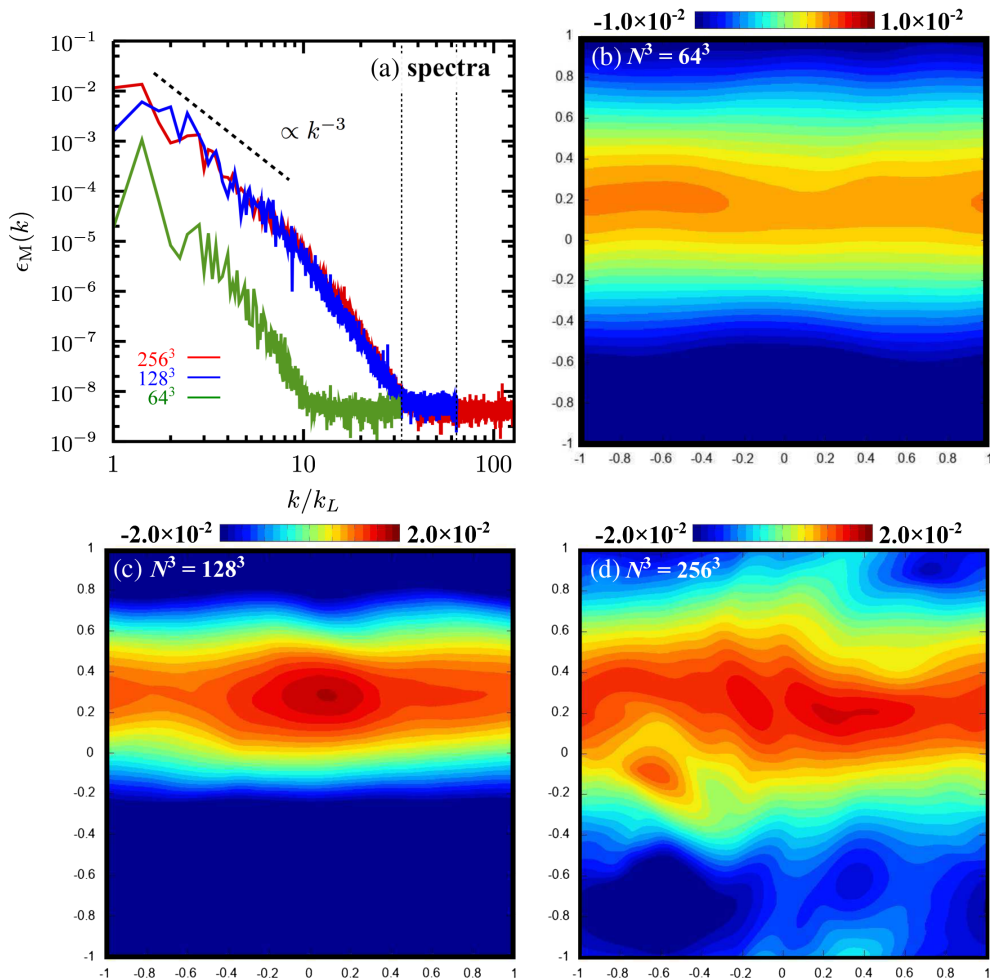

FIG. 9.   (a) $\epsilon_M(k)$ for the models with different resolutions. The dashed line is a reference slope proportional to k^{-3}. The x–y distributions of B_x at the saturated stage for the models with (b) $N = 64^3$ (model 3), (c) 128^3 (model 2), and (d) 256^3 (model 1).

provides the critical wavelength of the CPI comparable to the box size of each model, $\lambda_{\mathrm{crit}} = 2\pi/\xi_{B,\mathrm{sat}} \simeq L$. In Fig. 14, we can indeed confirm that the spatial structure of the magnetic field is comparable to the domain size. All these results verify our hypothesis that $\xi_{B,\mathrm{sat}}$ is restricted

numerically by the calculation domain and furthermore implies that the structures of $\boldsymbol{B}$ and $\boldsymbol{v}$ can evolve to the macroscopic scale comparable to the size of the PNS if we can enlarge the simulation domain to the system scale with keeping the sufficient resolution.
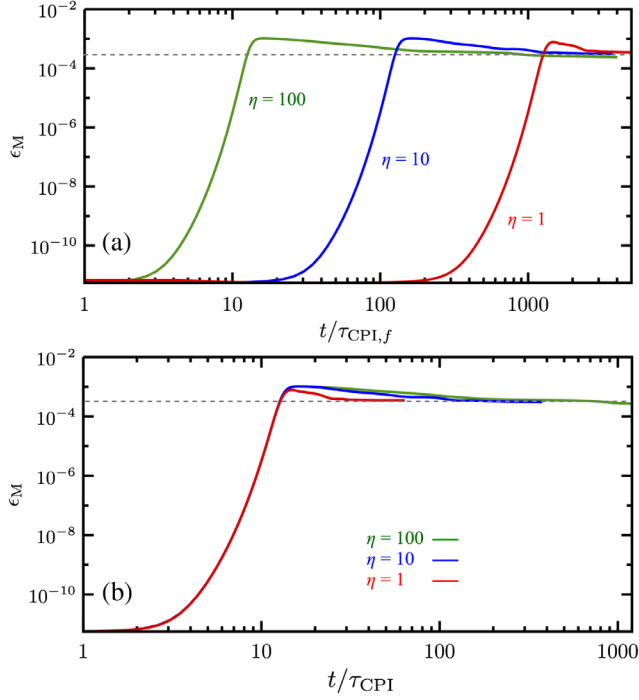
FIG. 10. Temporal evolutions of ϵ_M for the models with different values of η. The red, blue, and green lines correspond to the models with $\eta = 1$, 10, and 100, respectively. The normalization of the horizontal axis is different between panels (a) and (b). In panel (a), the horizontal axis is normalized by $\tau_{\mathrm{CPI,f}}$. In panel (b), the normalization unit is τ_{CPI}.

F. Dependence on axial charge density

Finally, we study the dependence of the behavior of the chiral MHD turbulence on the initial value of n_A. Remember that n_A is directly related to ξ_B [see Eq. (9)], and thus it is the most important parameter in
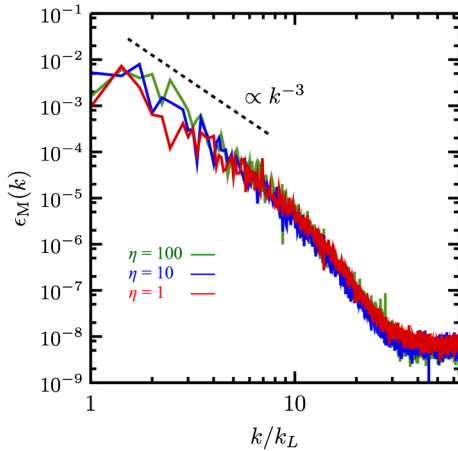
FIG. 11. $\epsilon_M(k)$ at the saturated stage for the models with different values of η. The red, blue, and green lines correspond to the models with $\eta = 1$, 10, and 100, respectively. The dashed line is a reference slope proportional to k^{-3}.
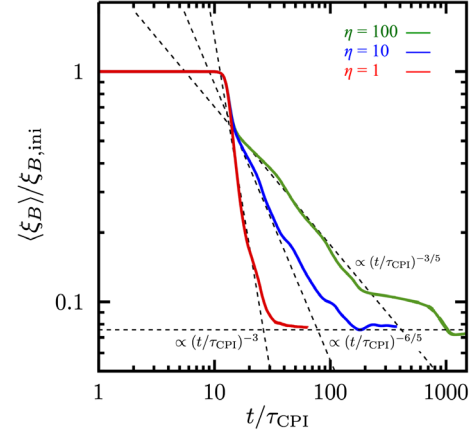
FIG. 12. Temporal evolutions of $\langle \xi_B \rangle$ normalized by $\xi_{B,\mathrm{ini}}$ for the models with different values of η. The red, blue, and green lines correspond to the models with $\eta = 1$, 10, and 100, respectively.

our simulation. In models 9 and 10, we set $n_A = 0.416$ and 0.020, i.e., $\xi_B = 5\xi_{B0}$ and $\xi_{B0}/5$, respectively. For a fair comparison between the models, we need to keep the ratio $L/\lambda_{\mathrm{crit}}$ constant because, as discussed in Sec. III E, $L/\lambda_{\mathrm{crit}}$ affects $\xi_{B,\mathrm{sat}}$ or the energy conversion efficiency. Therefore, the box sizes $L = L_0/5$ and $L = 5L_0$ are adopted for models 9 and 10, correspondingly. The other parameters are kept unchanged from model 5 with $\xi_B = \xi_{B0}$ and $L = L_0$.

Shown in Figs. 15(a) and 15(b) are the temporal evolutions of $\langle B^2 \rangle^{1/2}$ and $\langle \xi_B \rangle$ for these models. The blue, red, and green lines denote the models with $\xi_B = 5\xi_{B0}$, ξ_{B0}, and $\xi_{B0}/5$, respectively. Note that, in both panels, the simulation time is normalized by τ_{CPI} of each model. The vertical axis of the panel (b) is normalized by $\xi_{B,\mathrm{ini}}$ of each model.
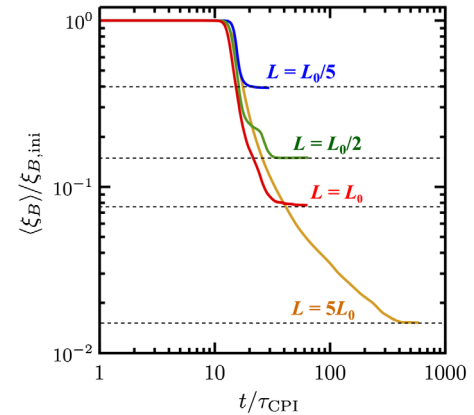

FIG. 13. Temporal evolutions of $\langle \xi_B \rangle$ for the models with the different box sizes. The blue, green, red, and orange lines denote the models with $L = 5L_0$, L_0, $L_0/2$, and $L_0/5$. The vertical axis is normalized by the initial value of $\langle \xi_B \rangle$ for each model.
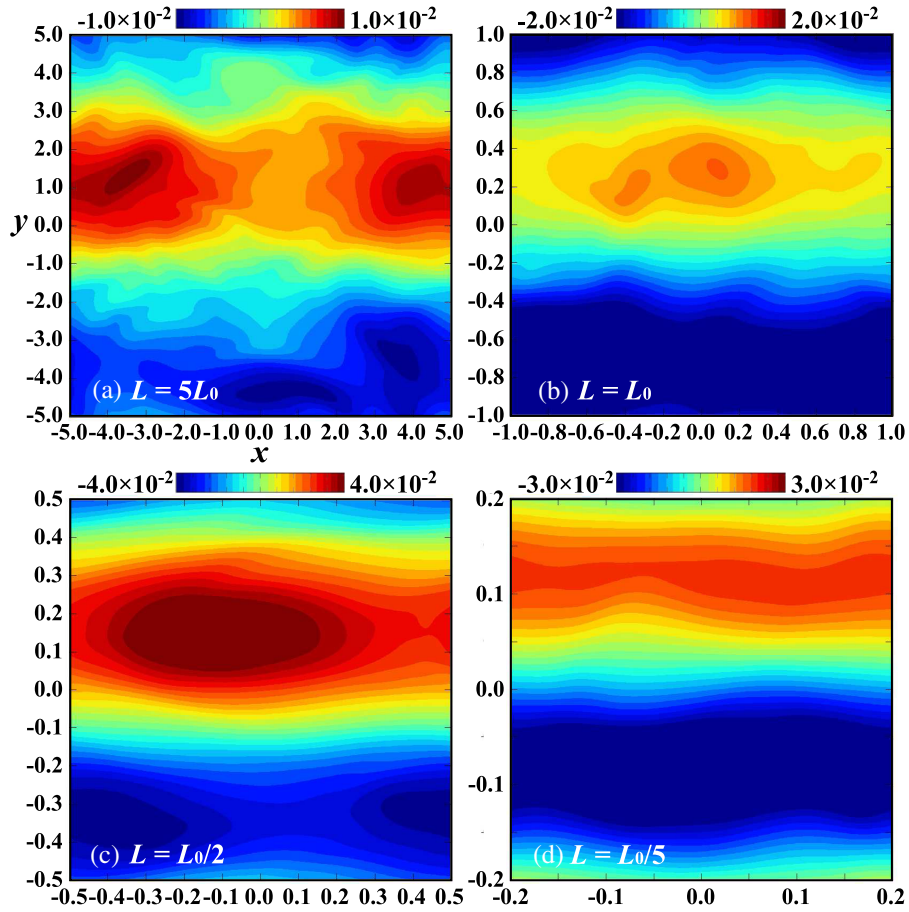
FIG. 14.   Distributions of B_x at the saturated stages on the x–y cutting plane at $z = 0$ for the models with (a) $L = 5L_0$, (b) $L = L_0$, (c) $L = L_0/2$, and (d) $L = L_0/5$. The axes are normalized by $L_0/2$ for all the models.

At the early stage $t \lesssim 10\tau_{\mathrm{CPI}}$, the evolution history of $\langle B^2 \rangle^{1/2}$ is consistent with the linear analysis of the CPI and does not depend on $\xi_{B,\mathrm{ini}}$. However, at the nonlinear stage, there exists a remarkable difference despite $\langle \xi_B \rangle / \xi_{B,\mathrm{ini}}$ being almost the same [see panel (b)]. We can evaluate $B_{\mathrm{sat}} \equiv \langle B^2(t_{\mathrm{sat}}) \rangle^{1/2}$ from the time average of $\langle B^2 \rangle^{1/2}$ at the nonlinear stage, as plotted in

Fig. 16 as a function of $\xi_{B,\mathrm{ini}}$. From this, we find the scaling relation,

$$B_{\mathrm{sat}} \propto \xi_{B,\mathrm{ini}}, \qquad (35)$$

indicating that the magnetic field strength maintained by the chiral MHD turbulence is a linear function of the total amount of $\xi_{B,\mathrm{ini}}$ generated in the supernova core.
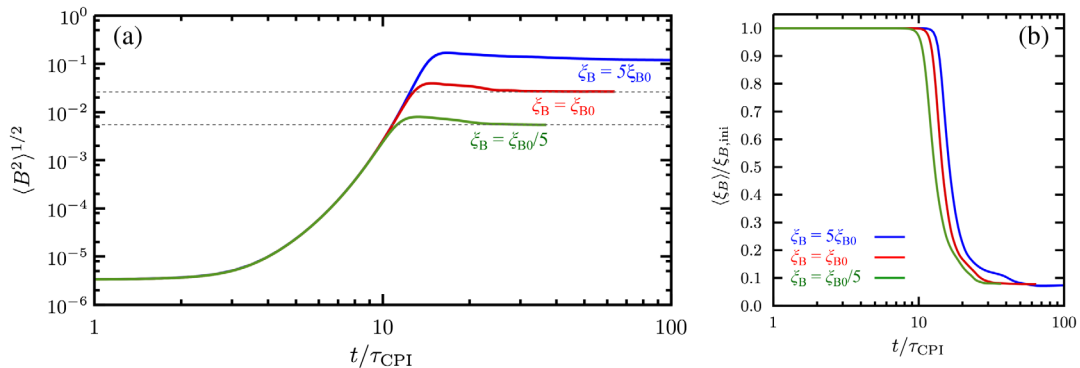

FIG. 15.   Temporal evolutions of (a) $\langle B^2 \rangle^{1/2}$ and (b) ξ_B for the models with the different initial values of n_A. The red, blue, and green lines denote the models with $\xi_{B,\mathrm{ini}} = 5\xi_{B0}$, ξ_{B0}, and $\xi_{B0}/5$.
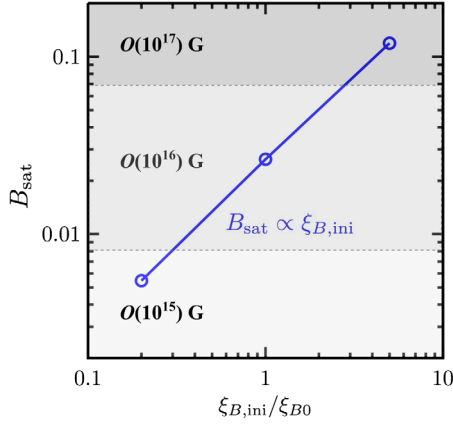
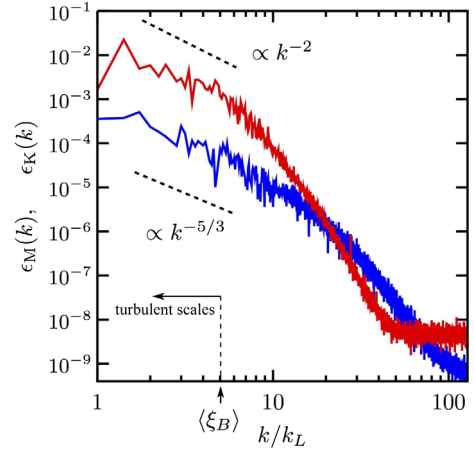FIG. 16. Scaling relation between B_{sat} and $\xi_{B,ini}$ normalized by the fiducial value ξ_{B0}.

FIG. 17. $\epsilon_M(k)$ (red) and $\epsilon_K(k)$ (blue) at $t = 300\tau_{CPI}$ before ϵ_K begins to decrease for the fiducial model. The arrow shows $\langle \xi_B \rangle$ at the corresponding time. The dashed lines are reference slopes proportional to k^{-2} and $k^{-5/3}$.

IV. DISCUSSION

A. Turbulence scaling

The spectrum of the chiral MHD turbulence was previously discussed for high-temperature plasmas in the early Universe in Ref. [31]. They observed the weak turbulence scaling with $\epsilon_M(k) \propto k^{-2}$ in the turbulent scales $k \lesssim \xi_B$ in the magnetically dominated turbulence, where the flow field is a consequence of driving by Lorentz force [68,69]. Note that our spectral scaling $\epsilon_M(k) \propto k^{-3}$ and $\epsilon_K(k) \sim k^{-2}$ in the low-k regime in Fig. 7(b) at the fully nonlinear stage is different from theirs.

The reason for this difference can be explained by the evolution of $\langle \xi_B \rangle$. While the spectrum in Ref. [31] is the case *before* $\langle \xi_B \rangle$ reaches the floor value, our spectra in Fig. 7(b) are derived *after* that, where $\lambda_{crit} \sim L$, and the turbulent scales are absent. Since the chiral MHD turbulence has smaller scales than the instability scale, its spectrum shows the steeper slope than in the turbulent scales.

Figure 17 shows the spectra of $\epsilon_M(k)$ and $\epsilon_K(k)$ before $\langle \xi_B \rangle$ reaches the floor value ($t \simeq 300\tau_{CPI}$) for the fiducial model. It can be seen that $\epsilon_M(k)$ is roughly proportional to k^{-2} in the range $k \lesssim \langle \xi_B \rangle$, as is consistent with the weak turbulence scaling discussed in Ref. [31]. In addition, we also observe that $\epsilon_K(k) \sim k^{-5/3}$ in this stage. This suggests that the chiral MHD turbulence has weak turbulence scalings, $\epsilon_M(k) \propto k^{-2}$ and $\epsilon_K(k) \propto k^{-5/3}$, in the regime $k \lesssim \langle \xi_B \rangle$ for high-density matter in the supernova core as well.

B. Chiral vortical effect

In this study, we have ignored the CVE just for simplicity. Including the CVE modifies the induction equation as [8]

$$\partial_t \boldsymbol{B} = \boldsymbol{\nabla} \times (\boldsymbol{v} \times \boldsymbol{B}) + \eta \nabla^2 \boldsymbol{B} + \eta \boldsymbol{\nabla} \times (\xi_B \boldsymbol{B} + \xi_\omega \boldsymbol{\omega}). \quad (36)$$

When taking account of the CVE, the energy reconversion from the flow field to the magnetic field is naively expected, because a helical flow field is generated as a consequence of the chiral transport phenomena [8]. The ratio ϵ_M/ϵ_K may be varied depending on ξ_ω.

In the actual PNS system, the CVE may provide significant change for the chiral MHD turbulence, since the helical and vortical flow motions should be excited not only locally but also globally through several macroscopic effects mainly due to the global rotation and the stratified structure; see, e.g., Refs. [57,59,60,70]. In the region with the magnetic field parallel to the vortical axis, the CVE should enhance the magnetic energy by the conversion from the fluid helicity to the magnetic helicity. In an opposite way, it should be possible that the magnetic energy is reduced by the CVE in the region with the magnetic field antiparallel to the vortical axis. A quantitative understanding of the CVE in the actual global system of the PNS is beyond the scope of this paper and is a target of our future work.

V. SUMMARY

In this paper, we have performed 3D numerical simulations of the chiral MHD turbulence, driven by the CPI, in the vicinity of the PNS in the supernova core. We adopted a local Cartesian model which zooms in on a small patch of the PNS. Our findings are summarized as follows.

(1) The magnetic field is amplified exponentially in accordance with the linear analysis of the CPI in the early evolutionary stage and then enters the nonlinear stage at around $t \simeq \mathcal{O}(10)\tau_{CPI}$. Not only the magnetic field but also the flow field coevolve due to the frozen-in property of the plasma and magnetic field. The kinetic energy of the chiral MHD

turbulence is an order of magnitude smaller than the magnetic one at the nonlinear stage.

(2) The magnetic and velocity fields exhibit the inverse energy cascade. While they have small-scale structures in the early evolutionary stage, they evolve to organize the large-scale structure with the spatial scale comparable to the size of the calculation domain. This conforms with what the linear analysis of the CPI predicts, i.e., the typical wavelength of the CPI is proportional to the chiral magnetic conductivity, $\lambda_{\mathrm{crit}} \propto \xi_B$, and it becomes longer as ξ_B decreases with time. At the saturated stage, the Fourier spectra of the magnetic and kinetic energy densities have slopes in proportion to k^{-3} and k^{-2}, respectively.

(3) Two numerical parameters impact the chiral MHD turbulence: one is the resolution, and the other is the box size. The sufficient condition for resolving the chiral MHD turbulence is $\lambda_{\mathrm{crit}}/\Delta \gtrsim 7$, where Δ is the grid size. While the lower resolution run provides the lower amplitude of the chiral MHD turbulence, the floor value of ξ_B is predominantly determined by the size of the calculation domain (less sensitive to the numerical resolution). The larger the size of the calculation domain is, the lower the floor value of ξ_B is. Therefore, the spatial structures of the magnetic and flow fields become larger with increasing the box size, implying that they can evolve to a macroscopic scale comparable to the size of the PNS if the calculation domain is enlarged to the system scale with keeping the sufficient resolution.

(4) One of the key physical parameters for the CPI is the resistivity η because the growth rate of the CPI becomes larger with increasing η. We found from the parametric study that the size of η does not have a significant impact on the chiral MHD turbulence itself, though the time required for the saturation of the CPI largely depends on it.

(5) The strength of the chiral MHD turbulence is essentially determined by the initial axial charge density. The scaling relation between the saturated value of the mean magnetic-field strength and the initial value of the chiral magnetic conductivity is given by $B_{\mathrm{sat}} \propto \xi_{B,\mathrm{ini}}$. This indicates that the magnetic-field strength maintained by the chiral MHD turbulence is a linear function of the total amount of ξ_B generated in the supernova core.

Our results suggest that the chiral effects of leptons would impact the dynamics of the PNS formation and supernova explosions by driving the strong MHD turbulence with the strong magnetic field. The next step of our study is modeling and taking account of the chiral effects into the global multidimensional MHD supernova simulations (e.g., Refs. [71,72]) to elucidate their dynamical impacts more quantitatively. In particular, it would be important to incorporate the contributions of the chiral transport of neutrinos [8], since they carry away most of the gravitational energy of an original massive star.

It should be remarked here that neutrinos are not always in thermal equilibrium, especially outside the supernova core, where hydrodynamics for neutrinos is not applicable. To take into account the effects of the left-handed-ness of neutrinos away from thermal equilibrium, one needs to use the so-called chiral kinetic theory [73–75], instead of the conventional kinetic theory (Boltzmann equation). Such a direction is deferred to future work.

ACKNOWLEDGMENTS

[1] M. Joyce and M. E. Shaposhnikov, Phys. Rev. Lett. **79,** 1193 (1997).

[2] A. Boyarsky, J. Frohlich, and O. Ruchayskiy, Phys. Rev. Lett. **108,** 031301 (2012).

[3] D. E. Kharzeev, J. Liao, S. A. Voloshin, and G. Wang, Prog. Part. Nucl. Phys. **88,** 1 (2016).

[4] J. Charbonneau and A. Zhitnitsky, J. Cosmol. Astropart. Phys. 08 (2010) 010.

[5] Y. Akamatsu and N. Yamamoto, Phys. Rev. Lett. **111,** 052002 (2013).

[6] A. Ohnishi and N. Yamamoto, arXiv:1402.4760.

[7] M. Kaminski, C. F. Uhlemann, M. Bleicher, and J. Schaffner-Bielich, Phys. Lett. B **760,** 170 (2016).

[8] N. Yamamoto, Phys. Rev. D **93,** 065017 (2016).

[9] H. B. Nielsen and M. Ninomiya, Phys. Lett. **130B,** 389 (1983).

[10] X. Wan, A. M. Turner, A. Vishwanath, and S. Y. Savrasov, Phys. Rev. B **83**, 205101 (2011).

[11] A. A. Burkov and L. Balents, Phys. Rev. Lett. **107**, 127205 (2011).

[12] G. Xu, H. Weng, Z. Wang, X. Dai, and Z. Fang, Phys. Rev. Lett. **107**, 186806 (2011).

[13] A. Vilenkin, Phys. Rev. D **22**, 3080 (1980).

[14] A. Y. Alekseev, V. V. Cheianov, and J. Frohlich, Phys. Rev. Lett. **81**, 3503 (1998).

[15] K. Fukushima, D. E. Kharzeev, and H. J. Warringa, Phys. Rev. D **78**, 074033 (2008).

[16] A. Vilenkin, Phys. Rev. D **20**, 1807 (1979).

[17] D. Kharzeev and A. Zhitnitsky, Nucl. Phys. **A797**, 67 (2007).

[18] D. T. Son and P. Surówka, Phys. Rev. Lett. **103**, 191601 (2009).

[19] K. Landsteiner, E. Megias, and F. Pena-Benitez, Phys. Rev. Lett. **107**, 021601 (2011); Lect. Notes Phys. **871**, 433 (2013).

[20] S. Adler, Phys. Rev. **177**, 2426 (1969).

[21] J. S. Bell and R. Jackiw, Nuovo Cimento A **60**, 47 (1969).

[22] M. Giovannini, Phys. Rev. D **88**, 063536 (2013).

[23] A. Boyarsky, J. Frohlich, and O. Ruchayskiy, Phys. Rev. D **92**, 043004 (2015).

[24] N. Yamamoto, Phys. Rev. D **93**, 125016 (2016).

[25] I. Rogachevskii, O. Ruchayskiy, A. Boyarsky, J. Fröhlich, N. Kleeorin, A. Brandenburg, and J. Schober, Astrophys. J. **846**, 153 (2017).

[26] K. Hattori, Y. Hirono, H. U. Yee, and Y. Yin, arXiv: 1711.08450.

[27] P. Pavlović, N. Leite, and G. Sigl, Phys. Rev. D **96**, 023504 (2017).

[28] Y. Hirono, D. Kharzeev, and Y. Yin, Phys. Rev. D **92**, 125031 (2015).

[29] E. V. Gorbar, I. Rudenok, I. A. Shovkovy, and S. Vilchinskii, Phys. Rev. D **94**, 103528 (2016).

[30] J. Schober, I. Rogachevskii, A. Brandenburg, A. Boyarsky, J. Froehlich, O. Ruchayskiy, and N. Kleeorin, Astrophys. J. **858**, 124 (2018).

[31] A. Brandenburg, J. Schober, I. Rogachevskii, T. Kahniashvili, A. Boyarsky, J. Fröhlich, O. Ruchayskiy, and N. Kleeorin, Astrophys. J. **845**, L21 (2017).

[32] J. Schober, A. Brandenburg, I. Rogachevskii, and N. Kleeorin, arXiv:1803.06350.

[33] M. Hongo, Y. Hirono, and T. Hirano, Phys. Lett. B **775**, 266 (2017).

[34] Y. Hirono, T. Hirano, and D. E. Kharzeev, arXiv:1412.0311.

[35] Y. Jiang, S. Shi, Y. Yin, and J. Liao, Chin. Phys. C **42**, 011001 (2018).

[36] V. Galitski, M. Kargarian, and S. Syzranov, arXiv:1804 .09339.

[37] D. Grabowska, D. B. Kaplan, and S. Reddy, Phys. Rev. D **91**, 085035 (2015).

[38] D. B. Kaplan, S. Reddy, and S. Sen, Phys. Rev. D **96**, 016008 (2017).

[39] G. Sigl and N. Leite, J. Cosmol. Astropart. Phys. 01 (2016) 025.

[40] M. Dvornikov and V. B. Semikoz, Phys. Rev. D **91**, 061301 (2015).

[41] H.-T. Janka, T. Melson, and A. Summa, Annu. Rev. Nucl. Part. Sci. **66**, 341 (2016).

[42] D. Radice, E. Abdikamalov, C. D. Ott, P. Mösta, S. M. Couch, and L. F. Roberts, J. Phys. G **45**, 053003 (2018).

[43] F. Hanke, A. Marek, B. Muller, and H. T. Janka, Astrophys. J. **755**, 138 (2012).

[44] T. Takiwaki, K. Kotake, and Y. Suwa, Astrophys. J. **786**, 83 (2014).

[45] R. Kazeroni, B. K. Krueger, J. Gilet, T. Foglizzo, and D. Pomarède, Mon. Not. R. Astron. Soc. **480**, 261 (2018).

[46] R. H. Kraichnan, Phys. Fluids **10**, 1417 (1967).

[47] D. S. Balsara, T. Amano, S. Garain, and J. Kim, J. Comput. Phys. **318**, 169 (2016).

[48] Y. Neiman and Y. Oz, J. High Energy Phys. 03 (2011) 023.

[49] N. A. Krall and A. W. Trivelpiece, *Principles of Plasma Physics* (McGraw-Hill, New York, 1973).

[50] D. A. Gurnett and A. Bhattacharjee, *Introduction to Plasma Physics* (Cambridge University Press, Cambridge, England, 2005).

[51] D. T. Son and A. R. Zhitnitsky, Phys. Rev. D **70**, 074018 (2004).

[52] M. A. Metlitski and A. R. Zhitnitsky, Phys. Rev. D **72**, 045011 (2005).

[53] A. Avdoshkin, V. P. Kirilin, A. V. Sadofyev, and V. I. Zakharov, Phys. Lett. B **755**, 1 (2016).

[54] H. K. Moffatt, *Magnetic Field Generation in Electrically Conducting Fluids* (Cambridge University Press, Cambridge, England, 1978).

[55] E. N. Parker, *Cosmical Magnetic Fields: Their Origin and Their Activity* (Oxford University, Oxford, 1979).

[56] F. Krause and K.-H. Raedler, *Mean-Field Magnetohydro-dynamics and Dynamo Theory* (Pergamon, Oxford, 1980).

[57] A. Brandenburg and K. Subramanian, Phys. Rep. **417**, 1 (2005).

[58] A. Brandenburg, J. Plasma Phys. **84**, 735840404 (2018).

[59] Y. Masada and T. Sano, Astrophys. J. Lett. **794**, L6 (2014).

[60] Y. Masada and T. Sano, Astrophys. J. Lett. **822**, L22 (2016).

[61] M. Dvornikov and V. B. Semikoz, Phys. Rev. D **95**, 043538 (2017).

[62] T. Sano, S. Inutsuka, and S. M. Miyama, Numer. Astrophys. **240**, 383 (1999).

[63] Y. Masada, T. Takiwaki, K. Kotake, and T. Sano, Astrophys. J. Lett. **798**, L22 (2015).

[64] D. A. Clarke, Astrophys. J. **457**, 291 (1996).

[65] C. R. Evans and J. F. Hawley, Astrophys. J. **332**, 659 (1988).

[66] K. Kotake, T. Takiwaki, Y. Suwa, W. I. Nakano, S. Kawagoe, Y. Masada, and S. i. Fujimoto, Adv. Astron. **2012**, 428757 (2012).

[67] E. M. Rossi, P. J. Armitage, and K. Menou, Mon. Not. R. Astron. Soc. **391**, 922 (2008).

[68] S. Galtier, S. V. Nazarenko, A. C. Newell, and A. Pouquet, J. Plasma Phys. **63**, 447 (2000).

[69] A. Brandenburg, T. Kahniashvili, and A. G. Tevzadze, Phys. Rev. Lett. **114**, 075001 (2015).

[70] Y. Masada, K. Yamada, and A. Kageyama, Astrophys. J. **778**, 11 (2013).

[71] P. Mösta, S. Richers, C. D. Ott, R. Haas, A. L. Piro, K. Boydstun, E. Abdikamalov, C. Reisswig, and E. Schnetter, Astrophys. J. **785**, L29 (2014).

[72] M. Obergaulinger and M. Á. Aloy, Mon. Not. R. Astron. Soc. **469**, L43 (2017).

[73] D. T. Son and N. Yamamoto, Phys. Rev. Lett. **109**, 181602 (2012); Phys. Rev. D **87**, 085016 (2013).

[74] M. A. Stephanov and Y. Yin, Phys. Rev. Lett. **109**, 162001 (2012).

[75] J.-W. Chen, S. Pu, Q. Wang, and X.-N. Wang, Phys. Rev. Lett. **110**, 262301 (2013).